Available online at www.sciencedirect.com
ScienceDirect
Trans. Nonferrous Met. Soc. China 26(2016) 3219−3231
Transactions of Nonferrous Metals Society of China
www.tnmsc.cn

Effects of spinning rate on structures and electrochemical hydrogen storage performances of RE−Mg−Ni−Mn-based AB_2-type alloys

Yang-huan ZHANG[1,2], Wei ZHANG[1], Xi-ping SONG[3], Pei-long ZHANG[3], Yong-guo ZHU[3], Yan QI[2]

1. Key Laboratory of Integrated Exploitation of Baiyun Obo Multi-metal Resources, Inner Mongolia University of Science and Technology, Baotou 014010, China;
2. Department of Functional Material Research, Central Iron and Steel Research Institute, Beijing 100081, China;
3. Whole Win (Beijing) Materials Sci. & Tech. Co., Ltd., Beijing 100083, China

Received 8 December 2015; accepted 18 April 2016

Abstract: La was partially substituted by Ce with the aim of improving the electrochemical hydrogen storage performances of $La_{1-x}Ce_xMgNi_{3.5}Mn_{0.5}$ (x=0, 0.1, 0.2, 0.3, 0.4) alloys, and melt spinning technology was adopted to fabricate the alloys. The identification of XRD and SEM reveals that the experimental alloys consist of a major phase $LaMgNi_4$ and a secondary phase $LaNi_5$. The growth of spinning rate results in that the lattice constants and cell volume increase and the grains are markedly refined. The electrochemical measurement shows that the as-cast and spun alloys can obtain the maximum discharge capacities just at the first cycle without any activation needed. With the increase of spinning rate, the discharge capacities of the alloys first increase and then decline, whereas their cycle stabilities always grow. Moreover, the electrochemical kinetic performances of the alloys first increase and then decrease with spinning rate growing.

Key words: Ni−MH battery; hydrogen storage; melt spinning; discharge capacity; kinetics

1 Introduction

Recently, an authoritative survey report from the Ministry of Environmental Protection of China declared that automobile exhaust is the main culprit giving rise to the severe haze in Beijing. Also, it was reported that a quarter of the world total energy was consumed by transport [1] and globally about 23% CO_2 emission originates from vehicular waste gases through the combustion of fossil fuels [2]. Hence, to vigorously develop electric vehicle (EV) and the hybrid electric vehicle (HEV) is deemed to be an attractive strategy to reduce both fossil energy consumption and carbon dioxide emission. To develop new electrode materials with high capacity, long life and low cost is a key technical obstacle for the widespread application of the EV and HEV. Several hydrogen storage materials are thought to be candidates as the negative electrode of Ni−MH batteries, especially rare earth-based AB_5 and AB_2-type alloys have been large-scale commercialized, but none of them is satisfactory due to their relatively low specific capacity. As for comprehensive electrochemical properties, RE−Mg−Ni-based A_2B_7-type and AB_2-type alloys have been considered to be the most promising candidates as the negative electrode materials of Ni−MH battery on account of their higher discharge capacities (380−410 mA·h/g) and lower production cost, as reported by KADIR et al [3] and KOHNO et al [4]. GUÉNÉE et al [5] studied the structures of $LaMgNi_4$ and $NdMgNi_4$ alloys and found that the alloys have a cubic $MgCu_4Sn$ ($AuBe_5$-type) structure. WANG et al [6] synthesized a $LaMgNi_4$ alloy by mechanical milling and found the maximum discharge capacity of the alloy being about 400 mA·h/g. Although extensive research has recently been performed to achieve the goal of application as summarized by LIU et al [7] and ZHANG et al [8], the attempt was still frustrated by the poor cycle stability of the new alloy. Consequently, the production of the new type alloys as the negative electrode of Ni−MH battery has not been found in China.

Alloying and microstructure modification are acknowledged to be effective approaches for improving the hydrogen storage properties of La−Mg−Ni-based

Foundation item: Projects (51371094, 51471054) supported by the National Natural Science Foundation of China
Corresponding author: Yang-huan ZHANG; Tel: +86-10-62183115; Fax: +86-10-62187102; E-mail: zhangyh59@sina.com
DOI: 10.1016/S1003-6326(16)64454-0

alloy [9,10]. Particularly, the partial substitution of rare earth elements (Ce, Pr, Nd and Sm) for La and Co, Mn, Cu and Al for Ni can markedly ameliorate the electrochemical cycle stability of the alloys [11−13]. In addition, it is evidenced that the electrochemical performances of the alloys are very sensitive to their structures [14]. Our previous research results indicated that melt-spinning could dramatically refine the structure of the La−Mg−Ni system A_2B_7-type alloys and considerably improve their cycle stability [15]. Hence, we expect that the combination of an optimized Ce substitution amount with a proper melt spinning technique may obtain an alloy with high discharge capacity and good cycling stability.

It is documented that adding rare earth elements can significantly improve the corrosion resistance of an electrode material, so as to improve its electrochemical properties, especially the cycle stability [16]. However, the full effect of elemental substitution on the hydrogen storage properties of La−Mg−Ni-based AB_2-type alloy remains unknown. In the present work, Ce was adopted to partially substitute La because Ce is cheaper and more abundant in reserve than Y or other rare earth elements, and melt spinning technology was used to fabricate the $La_{1-x}Ce_xMgNi_{3.5}Mn_{0.5}$ (x=0−0.4) alloys. Subsequently, the effects of spinning rate on the structure and electrochemical hydrogen storage characteristics of the alloys were investigated in detail. Our findings provide new insights into the capacity degradation mechanism of La−Mg−Ni system AB_2-type hydrogen storage alloys that may improve their cycling stability.

2 Experimental

The compositions of the experimental alloys were $La_{1-x}Ce_xMgNi_{3.5}Mn_{0.5}$ (x=0, 0.1, 0.2, 0.3, 0.4). For convenience, the alloys were denoted with Ce content as Ce_0, $Ce_{0.1}$, $Ce_{0.2}$, $Ce_{0.3}$ and $Ce_{0.4}$, respectively. The as-cast alloys were prepared by vacuum induction melting with the protection of helium atmosphere under a pressure of 0.04 MPa. Then, the as-cast alloys were spun with a water-cooled rotating copper roller. The spinning rate was expressed by the linear velocity of the copper roller. In the present experiment, the spinning rates were 2, 6, 10 and 15 m/s, respectively.

The phase compositions and structures of the as-cast and spun alloys were evaluated by X-ray diffraction (XRD) (D/max/2400) with a scan rate of 4 (°)/min. Before the XRD testing, the alloys were mechanically ground into powders with size less than 300 μm. The morphologies of the alloys were examined by a scanning electron microscopy (SEM) (QUANTA 400) attached with an energy disperse spectroscopy (EDS).

The electrochemical performances were evaluated by using a tri-electrode open cell at 303 K. Metal hydride electrodes were prepared by pressing the alloy powders and carbonyl nickel powders at a mass ratio of 1:4. The total mass was about 1 g, and the diameter was 15 mm. A sintered $Ni(OH)_2$/NiOOH counter electrode, a Hg/HgO reference electrode and the prepared metal hydride electrode were immersed in 6 mol/L KOH electrolyte. The charge/discharge cycles were carried out with a LAND (CT2001A) battery test instrument. In every cycle, the experimental cells were charged at the current density followed by a rest for 10 min, and then were discharged at the same current density to cut off voltage of −0.5 V.

The electrochemical impedance spectra (EIS) and the Tafel polarization curves of the alloys were measured using an electrochemical workstation (PARSTAT 2273). The fresh electrodes were fully charged and then rested for 2 h up to the stabilization of the open circuit potential. The EIS values of the alloy electrodes were measured at 50% depth of discharge (DOD), in frequency range from 10 kHz to 5 mHz, at amplitude of signal potentiostatic or galvanostatic measurements being 5 mV and the number of points per decade of frequencies being 60. The Tafel polarization curves were measured in the potential range from −1.2 to 1.0 V (vs Hg/HgO) with a scan rate of 5 mV/s. For the potentiostatic discharge, the test electrodes in the fully charged state were discharged at potential steps of 500 mV for 5000 s on electrochemical workstation, using an electrochemistry corrosion software (CorrWare).

3 Results and discussion

3.1 Microstructure characteristics

Figure 1 shows the XRD profiles of the as-cast and spun $La_{1-x}Ce_xMgNi_{3.5}Mn_{0.5}$ (x=0−0.4) alloys. It reveals that the as-cast and spun alloys have biphasic structures with a major phase $LaMgNi_4$ corresponding to cubic $SnMgCu_4$ ($AuBe_5$)-type structure with $F\bar{4}3m$ (216) space group and the secondary phase $LaNi_5$ corresponding to hexagonal $CaCu_5$-type structure with $P6/mmm$ (191) space group. Also, it is noted that the diffraction profiles are similar and exhibit sharp peaks, indicating excellent crystallinities and long-range crystallographic orders of the alloys [17]. The melt spinning brings on an obvious variation in the phase abundances of the alloys without altering the phase composition. Table 1 shows the lattice parameters of the $LaMgNi_4$ and $LaNi_5$ phases in the as-cast and spun Ce_0 and $Ce_{0.2}$ alloys, which were calculated from the XRD data by Jade 6.0 software. It is evident that melt spinning makes the lattice constants and cell volumes of the $LaMgNi_4$ and $LaNi_5$ phases obviously increase, which is most likely associated with the lattice stress and crystal

lattice distortion resulting from melt spinning. Meanwhile, melt spinning gives rise to the increase of $LaMgNi_4$ phase and the decrease of $LaNi_5$ phase. A careful observation will find that, for each spinning rate, the lattice constants and cell volumes of the $Ce_{0.2}$ alloy are visibly smaller than those of the Ce_0 alloy, which is ascribed to the fact that the atom radius of Ce is smaller than that of La.

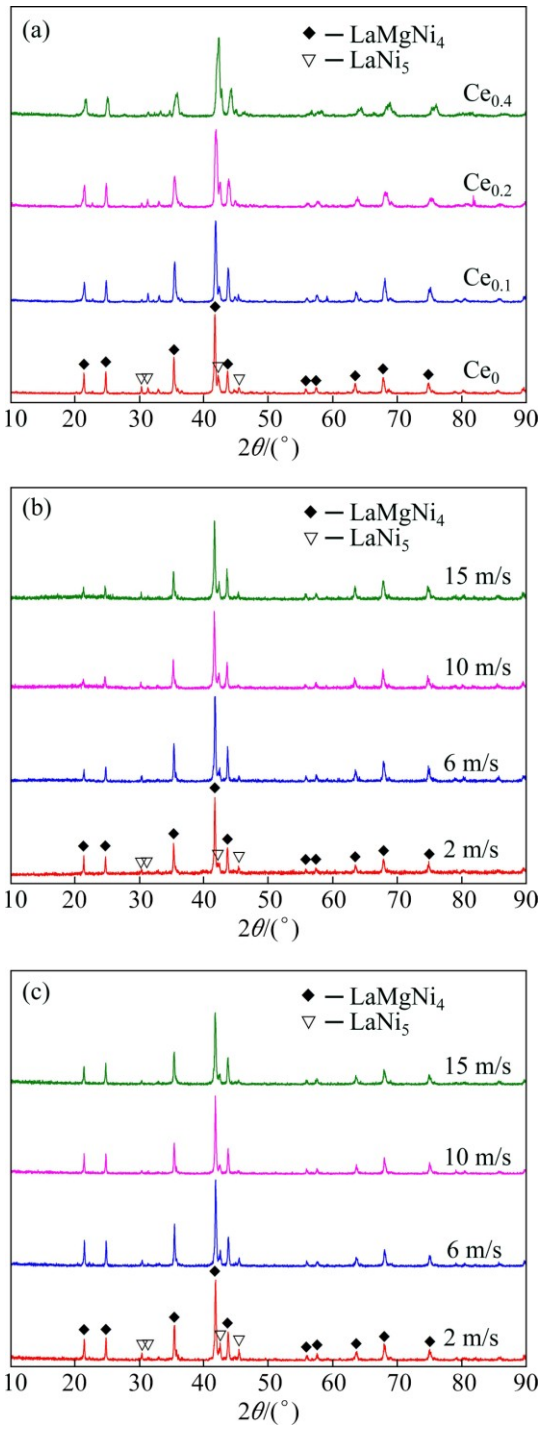

Fig. 1 XRD patterns of as-cast and spun $La_{1-x}Ce_xMgNi_{3.5}Mn_{0.5}$ (x=0−0.4) alloys: (a) As-cast alloys; (b) As-spun Ce_0 alloy; (c) As-spun $Ce_{0.2}$ alloy

The SEM images and EDS patterns of the as-cast Ce_0 and $Ce_{0.2}$ alloys are demonstrated in Fig. 2. Clearly, the morphologies of the as-cast alloys display typical dendritic structures. Two regions with different colors, bright and grey regions are found in the images. The analysis of EDS identifies that the grey region is $LaMgNi_4$ phase and the bright region is $LaNi_5$ phase, which conforms well to the XRD detection. Moreover, it is also observed that the substitution of Ce for La makes the alloy grains obviously refined.

The morphologies of the as-spun Ce_0 and $Ce_{0.2}$ alloys are presented in Fig. 3. Apparently, the grain sizes of the as-spun alloys markedly decrease with the increase of spinning rate. A particularly obvious characteristic can be found by comparing Figs. 2 and 3 that the melt spinning results in dramatic refinement of alloy grains. Moreover, it is noted that the as-spun Ce_0 and $Ce_{0.2}$ alloys exhibit different morphologies. The as-spun Ce_0 alloy shows a lath-like morphology. For $Ce_{0.2}$ alloy, by contrast, shows a feather-like morphology, and the grain sizes of the alloys at the same spinning rate also decrease with the Ce substitution.

3.2 Electrochemical performances

3.2.1 Activation capability, discharge capacity and potential characteristic

Figure 4 shows the variation of the discharge capacities of the as-cast and spun Ce_0 and $Ce_{0.2}$ alloys with cycle number at a current density of 60 mA/g. Obviously, the experimental alloys exhibit excellent activation performance, yielding their maximum discharge capacities just at the first charging−discharging cycle without any activation needed. The variation of spinning rate has no effect on the activation capability of the alloys. The activation capability of an alloy electrode directly depends on the change of the internal energy of the hydride system before and after absorbing hydrogen. The larger the added internal energy is, involving the surface energy originating from oxidation film formed on the surface of the electrode alloy and the strain energy resulting from hydrogen atom entering the interstitial sites of the tetrahedron or octahedron of the alloy lattice, the poorer the activation performance of the alloy will be [18]. The superior activation performance of the as-cast and spun alloys is principally attributed to their multiphase structures owing to the fact that the phase boundary can be viewed as the buffer zone to relieve the lattice distortion and strain energy formed in the process of hydrogen absorption. The refinement of the alloy grains caused by melt spinning is doubtlessly beneficial to improve the activation performance of the alloy.

Figure 5 describes the relationship between the discharge capacity of the $La_{1-x}Ce_xMgNi_{3.5}Mn_{0.5}$ (x=0−0.4) alloys and spinning rate. It is obvious that the discharge

Table 1 Lattice constants and abundances of $LaMgNi_4$ and $LaNi_5$ phases

Alloy	State	Phase	Lattice constant		Cell volume, V/nm^3	Phase abundance/%
			a/nm	c/nm		
Ce_0	As-cast	$LaMgNi_4$	0.7189	–	0.3715	76.5
		$LaNi_5$	0.5084	0.4021	0.0900	23.5
	As-spun at 2 m/s	$LaMgNi_4$	0.7191	–	0.3719	77.3
		$LaNi_5$	0.5086	0.4022	0.0901	22.7
	As-spun at 6 m/s	$LaMgNi_4$	0.7192	–	0.3720	77.9
		$LaNi_5$	0.5087	0.4024	0.0902	22.1
	As-spun at 10 m/s	$LaMgNi_4$	0.7194	–	0.3723	78.3
		$LaNi_5$	0.5088	0.4026	0.0903	21.7
	As-spun at 15 m/s	$LaMgNi_4$	0.7194	–	0.3723	78.5
		$LaNi_5$	0.5090	0.4028	0.0904	21.5
$Ce_{0.2}$	As-cast	$LaMgNi_4$	0.7184	–	0.3708	78.2
		$LaNi_5$	0.5079	0.4016	0.0898	21.8
	As-spun at 2 m/s	$LaMgNi_4$	0.7185	–	0.3709	78.9
		$LaNi_5$	0.5081	0.4019	0.0899	21.1
	As-spun at 6 m/s	$LaMgNi_4$	0.7186	–	0.3711	79.5
		$LaNi_5$	0.5082	0.4021	0.0899	20.5
	As-spun at 10 m/s	$LaMgNi_4$	0.7187	–	0.3712	79.6
		$LaNi_5$	0.5083	0.4023	0.0900	20.4
	As-spun at 15 m/s	$LaMgNi_4$	0.7189	–	0.3715	79.9
		$LaNi_5$	0.5084	0.4024	0.0901	20.1

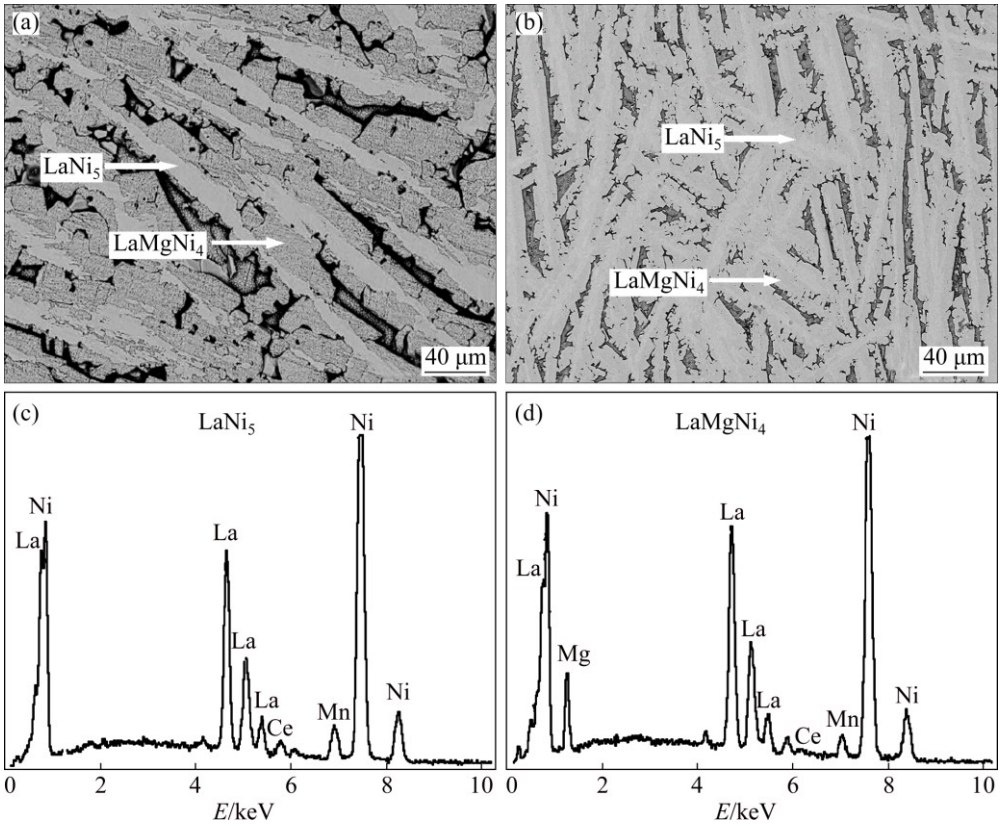

Fig. 2 SEM images together with typical EDS spectra of as-cast alloys: (a) Ce_0 alloy; (b) $Ce_{0.2}$ alloy; (c) EDS spectrum of $LaNi_5$ phase in $Ce_{0.2}$ alloy; (d) EDS spectrum of $LaMgNi_4$ phase in $Ce_{0.2}$ alloy

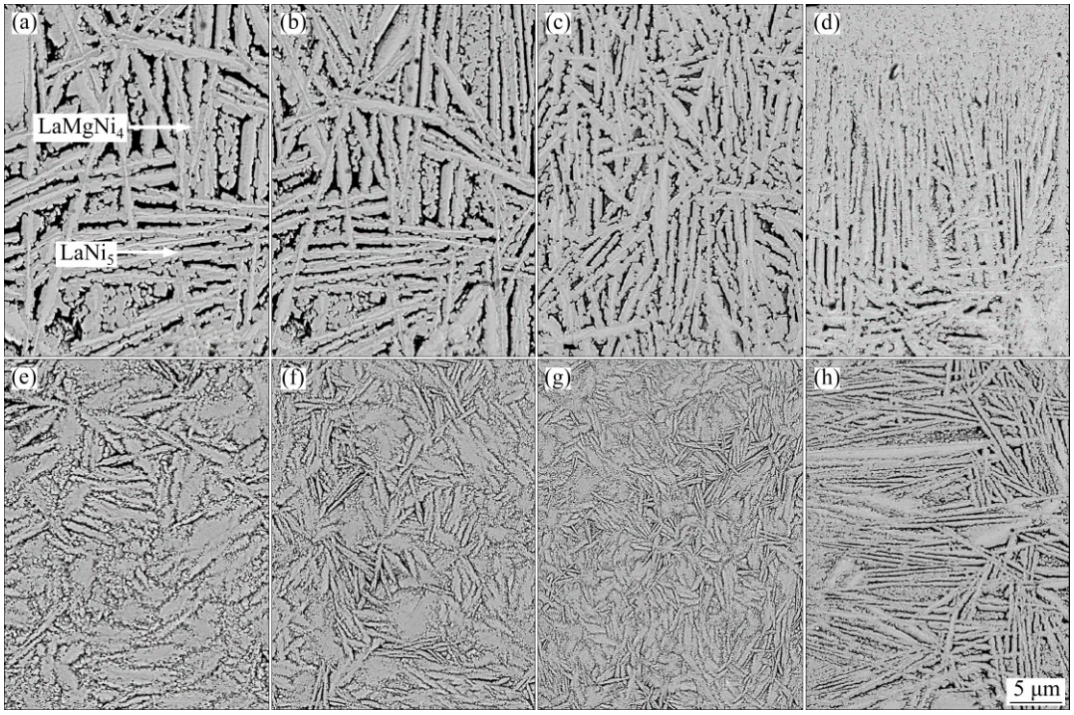

Fig. 3 SEM images of as-spun Ce_0 and $Ce_{0.2}$ alloys: (a−d) Ce_0 alloy spun at 2, 6, 10 and 15 m/s, respectively; (e−h) $Ce_{0.2}$ alloy spun at 2, 6, 10 and 15 m/s, respectively

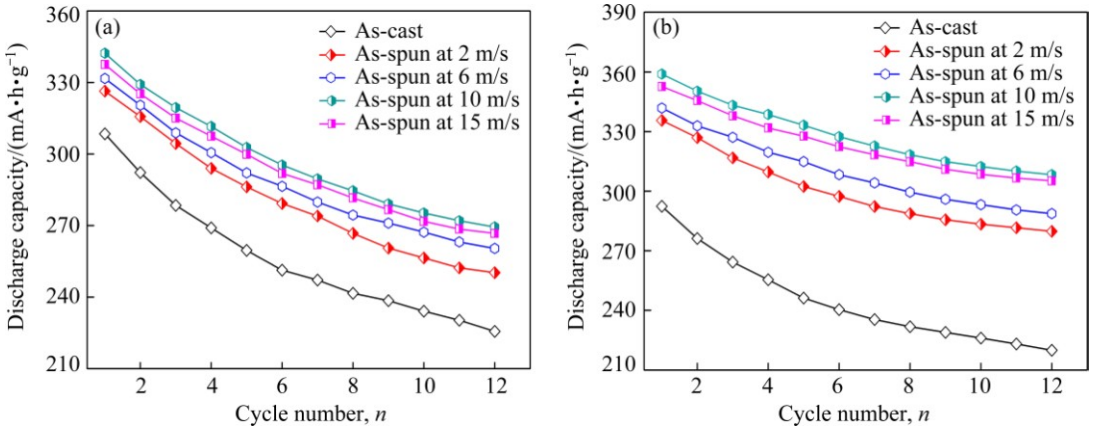

Fig. 4 Evolution of discharge capacity of as-cast and spun alloys with cycle number: (a) Ce_0 alloy; (b) $Ce_{0.2}$ alloy

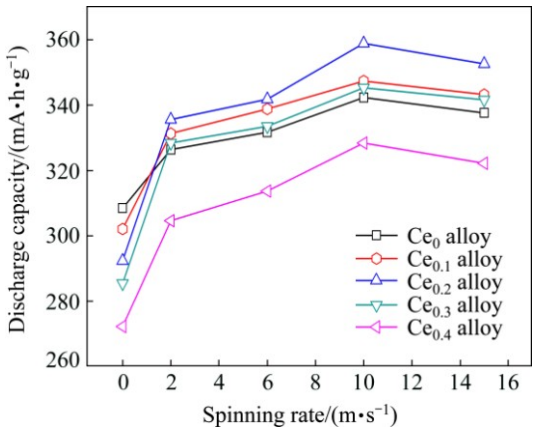

Fig. 5 Evolution of discharge capacity of as-cast and spun $La_{1-x}Ce_xMgNi_{3.5}Mn_{0.5}$ (x=0−0.4) alloys with spinning rate

capacities of the alloys first increase and then decrease with spinning rate growing. When the spinning rate is 10 m/s, the alloys yield the maximum discharge capacities, which are 342.3, 347.4, 358.9, 345.3 and 328.4 mA·h/g for the Ce_0, $Ce_{0.1}$, $Ce_{0.2}$, $Ce_{0.3}$ and $Ce_{0.4}$ alloys, respectively. The above results suggest that the melt spinning makes positive and negative actions on the discharge capacity of the alloys. The positive action is ascribed to the grains refined by melt spinning owing to the fact that the grain boundary exhibits the distribution of the maximum hydrogen concentrations [19]. As to the negative action, it is considered to be associated with the lattice stress generated by melt spinning. It can be inferred that the lattice stress is harmful to the discharge capacity of the alloys.

Figure 6 shows the discharge potential curves of the as-cast and spun Ce_0 and $Ce_{0.2}$ alloys at a current density of 60 mA/g. The discharge potential characteristic of an alloy is characterized by the potential plateau of the discharge curves. The longer and more horizontal the discharge potential plateau is, the better the discharge potential characteristic will be. Obviously, the experimental alloys show good potential characteristics, and the melt spinning notably ameliorates discharge potential characteristics of the alloys, enhancing discharge potential and lengthening discharge plateau. It is documented that the potential characteristic of an alloy is closely relevant to internal resistance of a battery, including ohmic internal resistance and polarization resistance, which basically depends on the diffusion of hydrogen atoms in the alloy and reduces with increasing diffusion coefficient [20]. The potential characteristic improved by melt spinning is most probably ascribed to the dramatic grain refinement due to the fact that grain boundaries may act as the fast diffusion paths for hydrogen atoms [21].

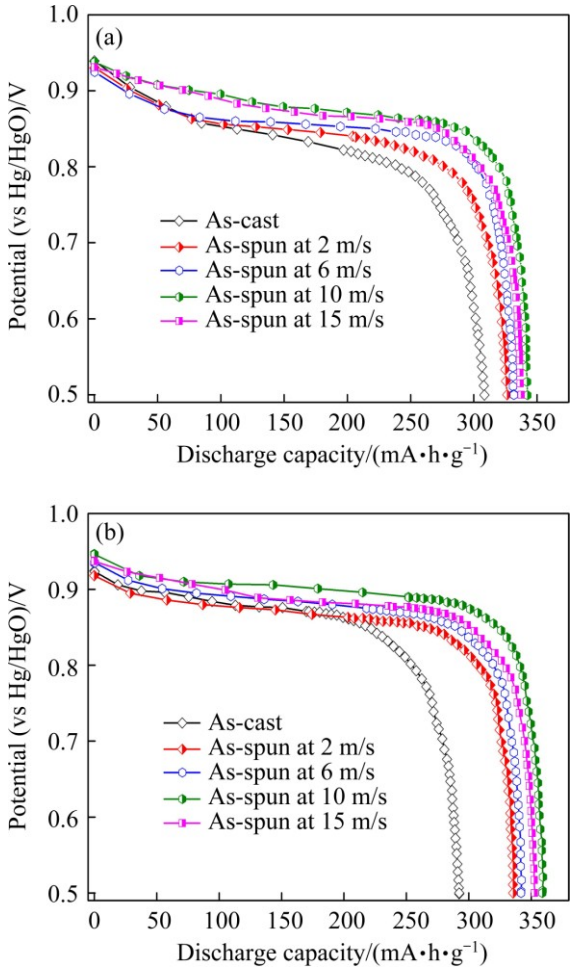

Fig. 6 Discharge potential curves of as-cast and spun $La_{1-x}Ce_xMgNi_{3.5}Mn_{0.5}$ (x=0−0.4) alloys: (a) Ce_0 alloy; (b) $Ce_{0.2}$ alloy

3.2.2 Electrochemical cycle stability

The electrochemical cycle stability of the experimental alloy electrodes is evaluated by capacity retaining rate (S_n), which is defined as $S_n=C_n/C_{max}\times100\%$, where C_{max} is the maximum discharge capacity and C_n is the discharge capacity of the nth charge−discharge cycle at a current density of 300 mA/g, respectively. The cycle stability of an alloy electrode is one of the major performance indicators that evaluate whether a kind of alloy can be applied as a negative electrode material of Ni−MH battery. Figure 7 illustrates the variation of the S_n values of the as-cast and spun Ce_0 and $Ce_{0.2}$ alloys with cycle number, which clearly displays the degradation process of the discharge capacity of the alloys. It is noted that the degradation rate of the discharge capacities of the as-cast and spun Ce_0 and $Ce_{0.2}$ alloys conspicuously decreases with spinning rate growing, meaning that the melt spinning generates a positive contribution to the cycle stability of the alloys. To directly reveal the effect of spinning rate on the cycle stability of the alloys, the relationship between the S_{150} (n=150) values and spinning rate is also inserted in Fig. 7. It is observed that the S_{150} values significantly increase with spinning rate growing. To be specific, the S_{150} value can be enhanced from 40.2% to 63.2% for the Ce_0 alloy and from 59.2% to 80.2% for the $Ce_{0.2}$ alloy by increasing spinning rate from 0 (as-cast is defined as the spinning rate of 0) to 15 m/s. A comparison shows that, for the same spinning rate, the $Ce_{0.2}$ alloy exhibits a much higher S_{150} value than the Ce_0 alloy, indicating that Ce substitution for La facilitates the improvement of the cycle stability of the alloy. It is well known that the primary causes leading to the capacity degradation of RE−Mg−Ni-based AB_2-type alloy are the pulverization and oxidation [22]. The hydrogen storage material suffers an inevitable volume expansion and contraction during the charge−discharge process, which aggravates the alloy's cracking and pulverizing. The fresh alloy surface contacting with the electrolyte will be oxidized, forming $La(OH)_2$ and $Mg(OH)_2$ surface layer, which is also evidenced by our experimental results, as demonstrated in Fig. 8. It is clear that there are many cracks on the surfaces of the alloy particles after electrochemical cycle. Meanwhile, it can be also seen that the alloy particles after cycling are covered by a rough and gossypine layer, which is identified to be $La(OH)_2$ and $Mg(OH)_2$ by XRD, as shown in Fig. 8(c). The positive contribution of melt spinning to the cycle stability of the alloys is ascribed to the grain refinement due to a well-known fact that the strength and toughness of an alloy increase with decreasing grain size. In other words, the smaller the size of alloy grain is, the better its strength and toughness are, and the higher the anti-pulverization capability is. With respect to the positive

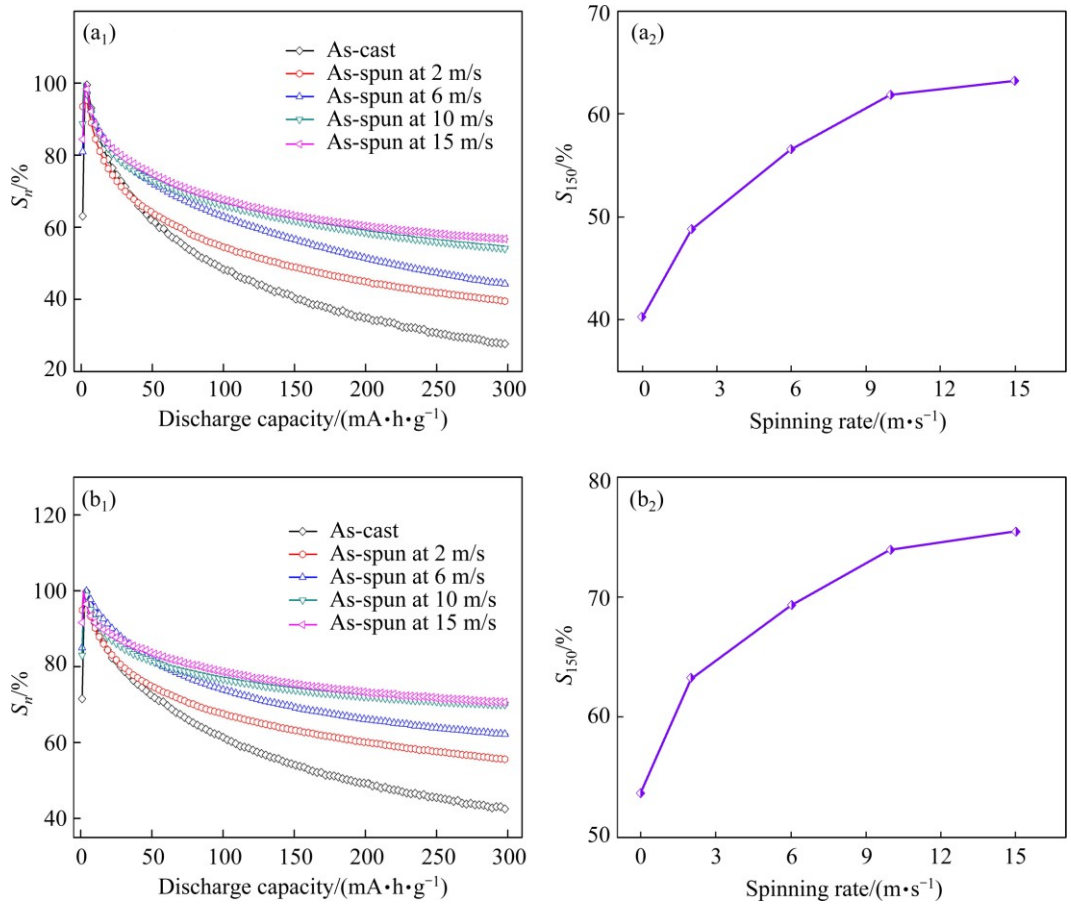

Fig. 7 Evolution of capacity retaining rate (S_n) and S_{150} vs spinning rate of as-cast and spun alloys: (a_1, a_2) Ce_0 alloy; (b_1, b_2) $Ce_{0.2}$ alloy

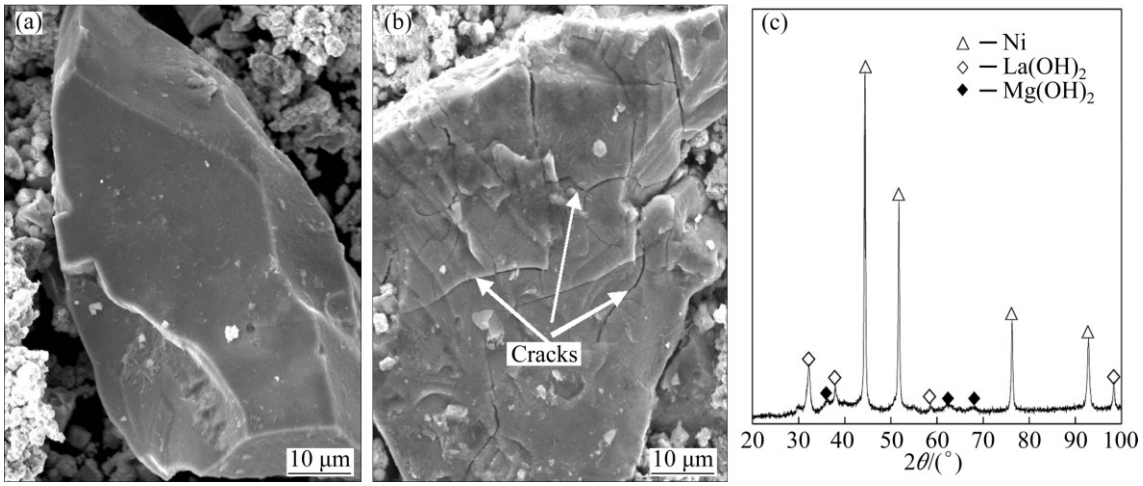

Fig. 8 SEM images (a, b) together with typical XRD pattern (c) of as-spun (10 m/s) $Ce_{0.2}$ alloy before (a) and after (b) electrochemical cycle

contribution of Ce substitution for La to cycle stability, it is considered to be affiliated with the enhancement of the anti-corrosion and anti-oxidation ability [23].

3.2.3 Electrochemical kinetics

The electrochemical kinetics of an alloy electrode is symbolized by high rate discharge ability (η_{HRD}), which is defined as: $\eta_{HRD}=C_J/C_{60}\times100\%$, where C_J and C_{60} are the maximum discharge capacities of the alloy electrode charged−discharged at the current densities of J and 60 mA/g, respectively. The current density dependence of the η_{HRD} values of the as-cast and spun Ce_0 and $Ce_{0.2}$ alloys is depicted in Fig. 9, from which it can be clearly seen that the η_{HRD} values of the as-cast and spun alloys markedly decline with current density growing. For

comparison, we take the current density of 300 mA/g as a criterion to set up the relationship between the η_{HRD} and spinning rate, as shown in Figs. 9(a_2) and (b_2), respectively. It is evident that the η_{HRD} values of the Ce_0 and $Ce_{0.2}$ alloys first increase and then decrease with spinning rate growing, and the maximum η_{HRD} is 92.9% for the Ce_0 alloy and 93.8% for the $Ce_{0.2}$ alloy, respectively, which are almost equal to the electrochemical kinetics of the rare earth-based AB_5-type alloy electrode.

It is well known that the η_{HRD} of an alloy electrode is basically dominated by hydrogen diffusion ability in the alloy bulk and charge-transfer rate on the alloy electrode surface [24]. To investigate the kinetic mechanism of the experimental alloys, the effects of spinning rate on the hydrogen diffusion ability and charge-transfer rate were studied. The semilogarithmic curves of anodic current versus the working duration of an alloy electrode were measured, as demonstrated in Fig. 10. Based on Ref. [25], the diffusion coefficient of hydrogen atoms in the bulk of an alloy could be easily calculated from the slope of the linear region of the corresponding plots according to the following formulae:

$$\lg J = \lg\left(\pm\frac{6FD}{da^2}(C_0 - C_s)\right) - \frac{\pi^2}{2.303}\frac{D}{a^2}t \quad (1)$$

$$D = -\frac{2.303a^2}{\pi^2}\frac{\mathrm{d}\lg J}{\mathrm{d}t} \quad (2)$$

where J is the diffusion current density (A/g), D is the hydrogen diffusion coefficient (cm^2/s), C_0 is the initial hydrogen concentration in the bulk of the alloy (mol/cm^3), C_s is the hydrogen concentration on the surface of the alloy particles (mol/cm^3), a is the alloy particle radius (cm), d is the density of the hydrogen storage alloy (g/cm^3), t is the discharge time (s). The D values calculated from Eq. (2) as a function of spinning rate are inserted in Figs. 10(a_2) and (b_2), respectively. Evidently, the D values of the alloys first augment and then decline with spinning rate increasing.

Limiting current density (J_L), another important parameter related to the diffusion ability of hydrogen atoms, can be derived by measuring the potentiodynamic polarization curve of an alloy electrode, as illustrated in Fig. 11. A clear inflection point can be found on each anodic polarization curve. The current density value corresponding to inflection point is termed as the limiting current density, which is viewed as an oxidation reaction taking place on the alloy electrode surface, and consequently the oxidation layer hindering hydrogen atoms from further penetrating [22]. Thus, the limiting current density (J_L) can be thought to be a critical current

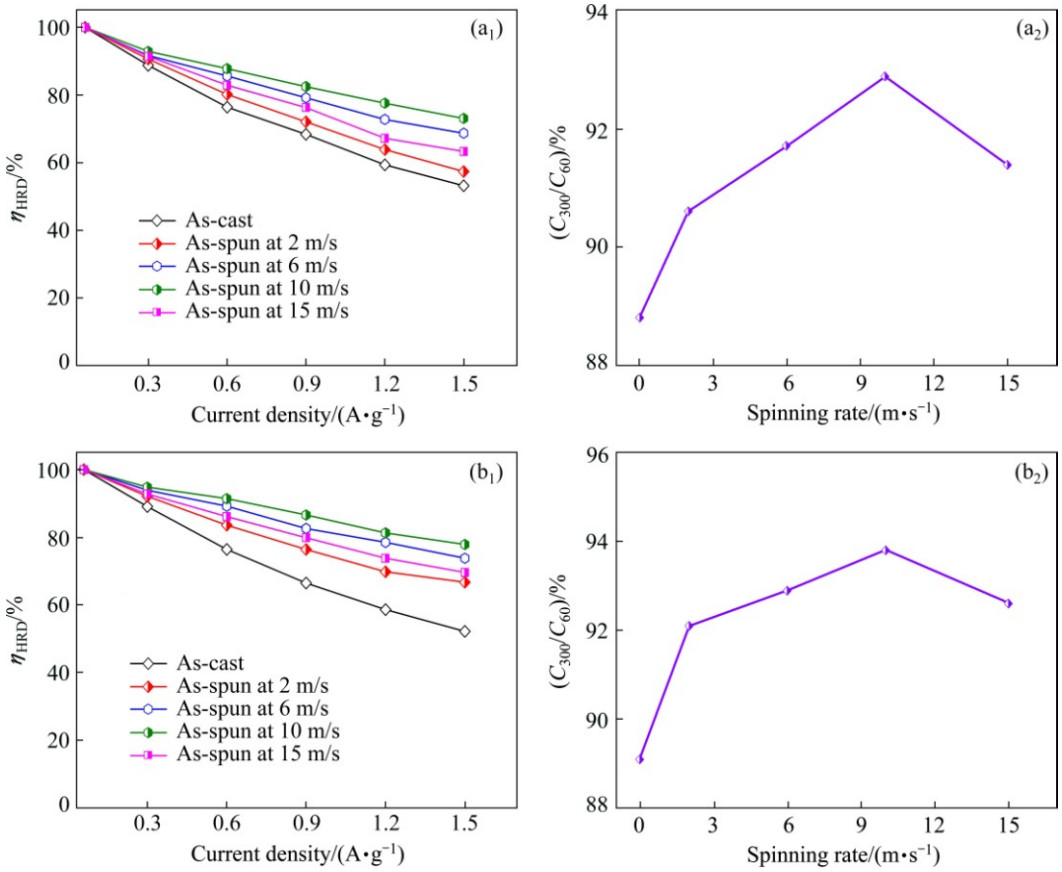

Fig. 9 Evolution of η_{HRD} (a_1, b_1) and C_{300}/C_{60} vs spinning rate (a_2, b_2) of as-cast and spun Ce_0 (a_1, a_2) and $Ce_{0.2}$ (b_1, b_2) alloys with current density

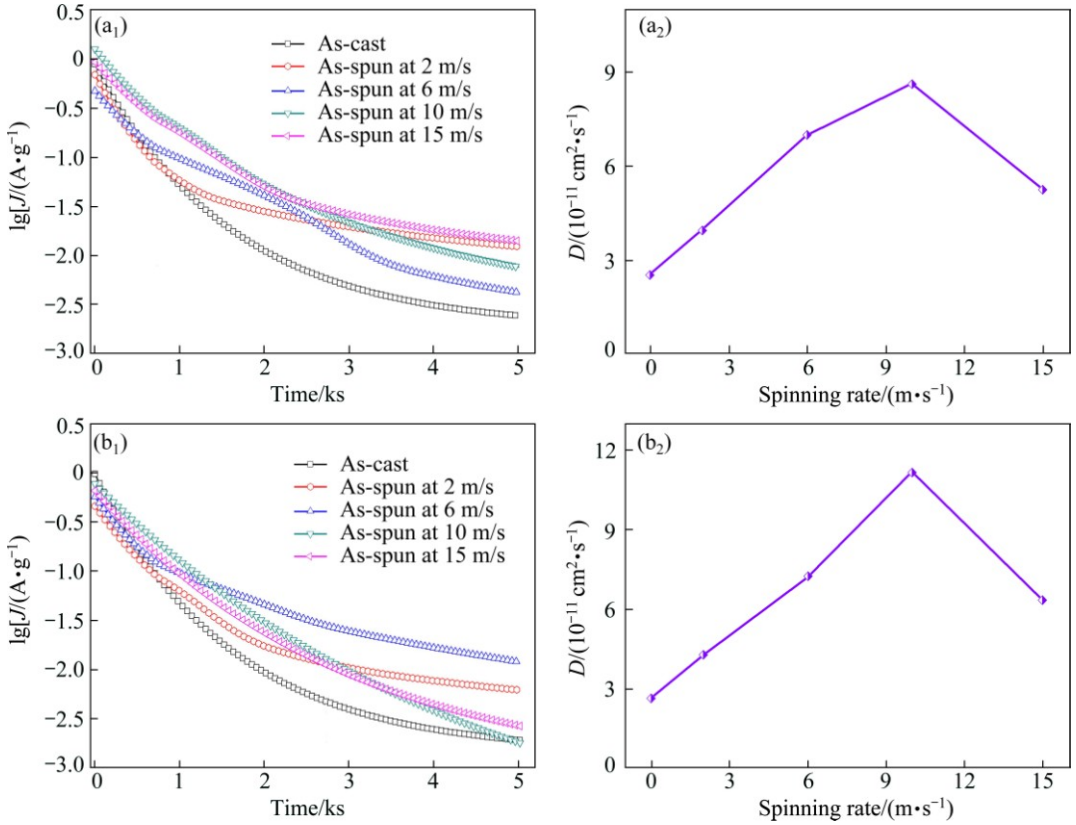

Fig. 10 Semilogarithmic curves of anodic current vs time responses (a_1, b_1) and D vs spinning rate curves (a_2, b_2) of as-cast and spun alloys: (a_1, a_2) Ce_0 alloy; (b_1, b_2) $Ce_{0.2}$ alloy

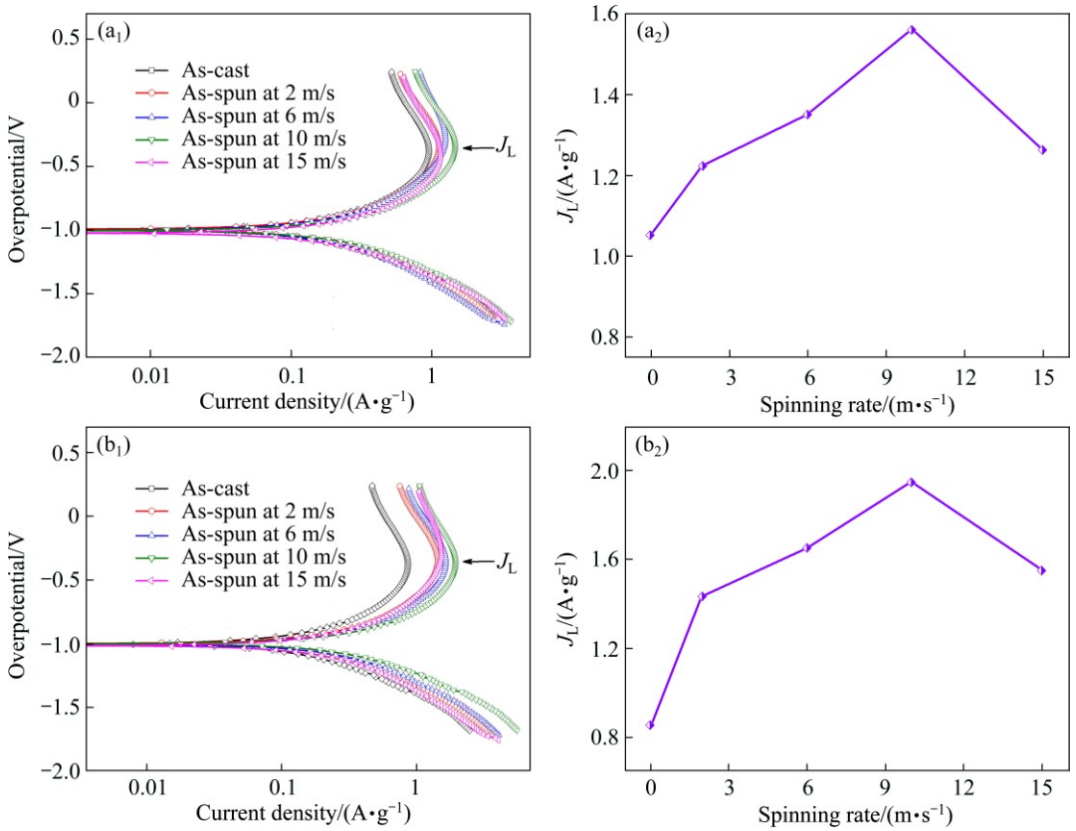

Fig. 11 Potentiodynamic polarization curves (a_1, b_1) and J_L vs spinning curves (a_2, b_2) of as-cast and spun alloys: (a_1, a_2) Ce_0 alloy; (b_1, b_2) $Ce_{0.2}$ alloy

density for passivating. Based on the data in Fig. 11, the relationships between the J_L values and spinning rate can be established, just as shown in Figs. 11(a_2) and (b_2), respectively. A comparison of Figs. 10 and 11 indicates that the variation tendencies of the D and J_L values with spinning rate are very similar, suggesting that two parameters factually reflect the diffusion ability of hydrogen atoms. In addition, it is also found that the variation trends of the D and J_L values of the alloys with spinning rate are very similar to that of the η_{HRD}, meaning that the diffusion ability of hydrogen atoms is a very important factor affecting the electrochemical kinetics of the alloy. The grain refined by Ce substitution for La evidently is facilitated. The positive action of melt spinning on the diffusion ability of hydrogen atoms is ascribed to the refinement of the alloy grains which was mentioned previously. The negative impact on hydrogen diffusion caused by melt spinning is most probably associated with lattice distortion, which will increase the diffusion activation energy of hydrogen atoms, consequently impairing hydrogen diffusion.

As for the charge-transfer rate on the alloy electrode surface, it can be determined from its electrochemical impedance spectrum (EIS) according to the Kuriyama model [26]. As a typical representative, the EIS curves of the as-cast and spun $Ce_{0.2}$ alloys are depicted in Fig. 12. It is evident that there are two distorted capacitive loops in the high and middle frequency regions separately as well as a line in the low frequency region in each EIS, which correctly reflects the electrochemical process of an alloy electrode. Among them, the smaller semicircle in the high frequency region represents the contact resistance between the alloy powder and the conductive material, and the larger one in the middle frequency region corresponds to the charge-transfer resistance (R_{ct}) on the alloy surface while the straight line in the low frequency region symbolizes Warburg impendence. By means of the equivalent circuit in Fig. 12, the R_{ct} values can be obtained with the fitting program Z-View. KURIYAMA et al [26] considered that the R_{ct} value principally depends on both the reactivity of the alloy surface and that of the reaction area. And the electrochemical reactivity of the alloy surface can be determined with apparent activation enthalpy $\Delta_r H^\Theta$, which can be obtained by the following equation:

$$\ln\left(\frac{T}{R_{ct}}\right) = C_0 - \frac{\Delta_r H^\Theta}{RT} \quad (3)$$

where R_{ct} is the charge-transfer resistance for the metal hydride electrodes, R is the gas constant, T is the temperature of the sample and C_0 is a constant of which

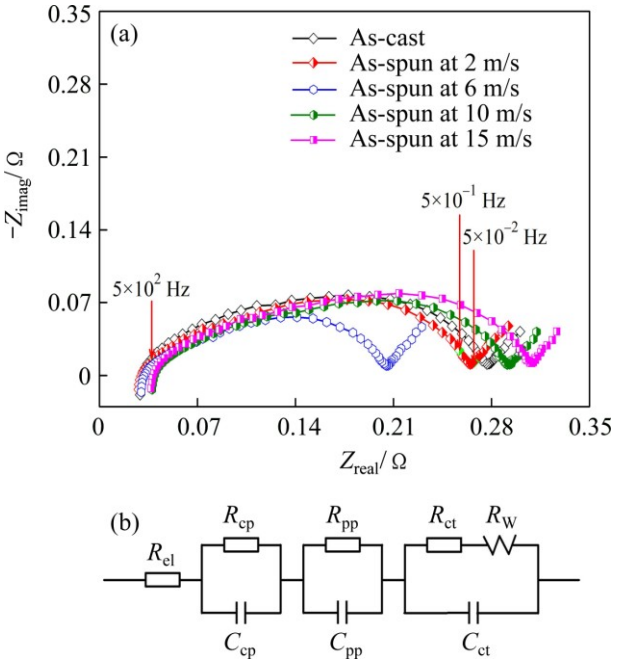

Fig. 12 Electrochemical impedance spectrum (EIS) of as-cast and spun $Ce_{0.2}$ alloy (a) and equivalent circuit (b)

the surface area is included. In view of the calculation conditions of Eq. (3), the EIS curves of the as-cast and spun $La_{1-x}Ce_xMgNi_{3.5}Mn_{0.5}$ (x=0−0.4) alloys are measured at different temperatures (303, 318 and 333 K), and as a representative, the EIS curves of the as-cast and spun Ce_0 and $Ce_{0.2}$ alloys are shown in Fig. 13. Based on the data in Fig. 13, the Kuriyama graphs of $\ln(T/R_{ct})$ vs $1/T$ can be plotted by using logarithmic transform of Eq. (3), as shown in Figs. 13(a_2) and (b_2), respectively. From the slopes of the Kuriyama plots, the $\Delta_r H^\Theta$ values can be easily calculated. Thus, the relationship between the $\Delta_r H^\Theta$ values and spinning rate is established, as described in Fig. 14. The $\Delta_r H^\Theta$ values of the alloys first decrease and then increase with spinning rate growing, namely there exists an optimal spinning rate at which the alloys possess the highest charge transfer rate. Thus, it can be inferred that the melt spinning plays beneficial and harmful roles in the charge transfer rate of the alloys. KLEPERIS et al [27] considered that the charge-transfer rate of an alloy electrode surface mainly depends on its crystallographic and electronic structure. The positive impact of the melt spinning on the charge transfer is most likely related to the crystallographic characteristics generated by melt spinning. As to the negative impact, it is considered to the ultra-refined grains by melt spinning because the refinement of the alloy grains greatly enhances the anti-pulverization ability of the alloy during electrochemical cycling, which means forming fewer fresh surface of the alloy, so as to inevitably impair the charge-transfer ability.

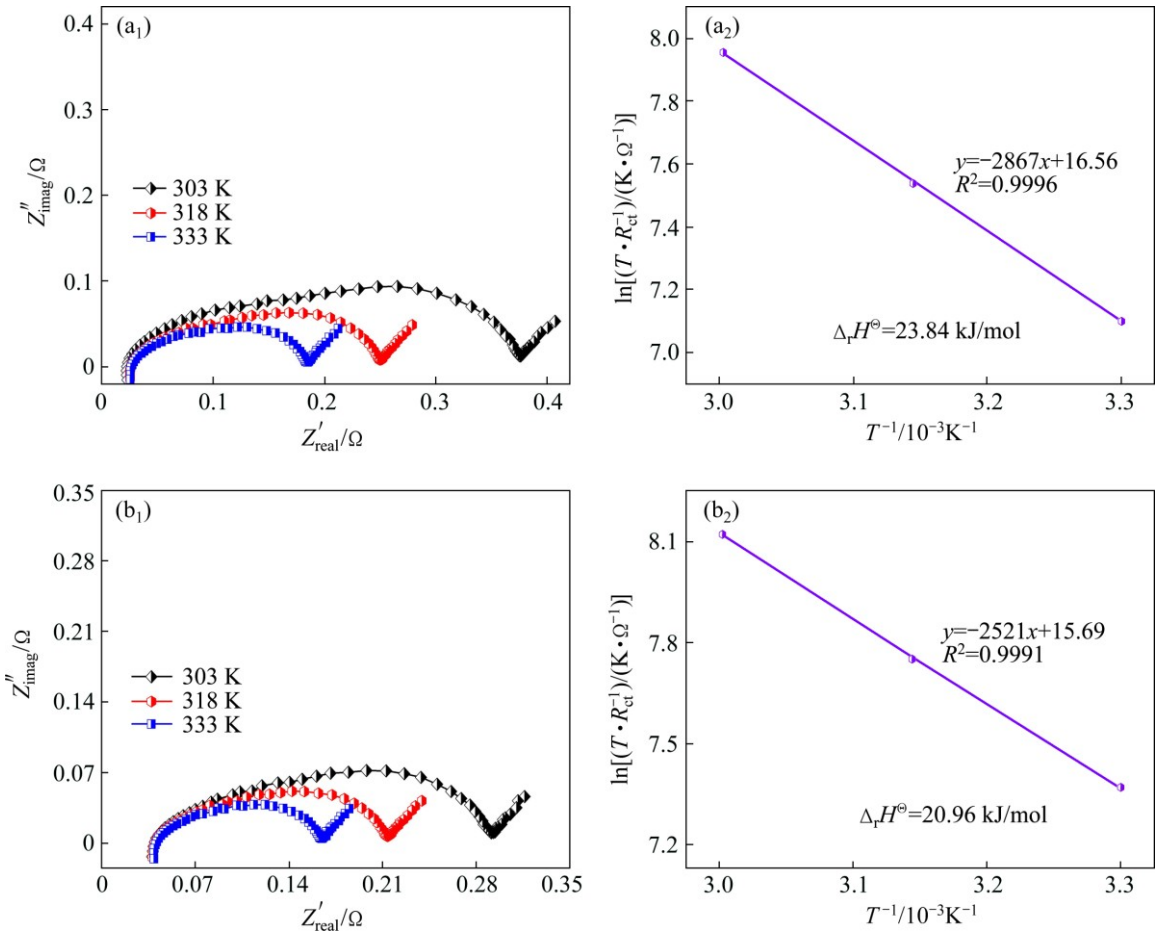

Fig. 13 Electrochemical impedance spectra (EIS) (a_1, b_1) and $\ln(T/R_{ct})$ vs T^{-1} curves (a_2, b_2) of as-spun (10 m/s) alloys at various temperatures: (a_1, a_2) Ce_0 alloy; (b_1, b_2) $Ce_{0.2}$ alloy

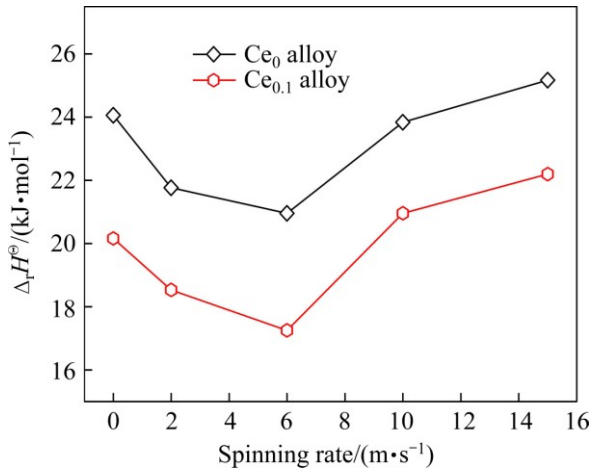

Fig. 14 Evolution of activation enthalpy $\Delta_rH^{\ominus}$ values of as-cast and spun Ce_0 and $Ce_{0.2}$ alloys with spinning rate

4 Conclusions

1) Melt spinning makes the dramatic refinement of the alloy grains. Meanwhile, it gives rise to increasing $LaMgNi_4$ phase and decreasing $LaNi_5$ phase without altering the phase compositions of the alloys. The lattice parameters and cell volumes of the experimental alloys visibly increase with spinning rate growing.

2) The as-cast and spun alloys exhibit excellent activation capability. The melt spinning can significantly improve the potential characteristics of the alloys. The discharge capacities of the alloys first increase and then decline with spinning rate rising. In addition, melt spinning can dramatically improve the electrochemical cycle stability of the alloys.

3) Electrochemical kinetics of the as-cast and spun alloys first increase and then decrease with spinning rate growing, for which the structure modified by melt spinning is principally responsible. The hydrogen diffusion coefficient (D) and the activation enthalpy ($\Delta_rH^{\ominus}$) of the alloys are thought to be the main controlling factors of the high rate discharge abilities (HRD) of the alloys.

References

[1] WANG N G, WANG R C, PENG C Q, HU C W, FENG Y, PENG B. Research progress of magnesium anodes and their applications in

chemical power sources [J]. Transactions of Nonferrous Metals Society of China, 2014, 24(8): 2427−2439.

[2] LAN R, IRVINE J T S, TAO S. Ammonia and related chemicals as potential indirect hydrogen storage materials [J]. International Journal of Hydrogen Energy, 2012, 37(2): 1482−1494.

[3] KADIR K, NORÉUS D, YAMASHITA I. Structural determination of $AMgNi_4$ (where A=Ca, La, Ce, Pr, Nd and Y) in the $AuBe_5$ type structure [J]. Journal of Alloys and Compounds, 2002, 345(1−2): 140−143.

[4] KOHNO T, YOSHIDA H, KAWASHIMA F, INABA T, SAKAI I, YAMAMOTO M. Hydrogen storage properties of new ternary system alloys: La_2MgNi_9, $La_5Mg_2Ni_{23}$, $La_3Mg_2Ni_{14}$ [J]. Journal of Alloys and Compounds, 2000, 311(2): L5−L7.

[5] GUÉNÉE L, FAVER-NICOLIN V, YVON K. Synthesis, crystal structure and hydrogenation properties of the ternary compounds $LaNi_4Mg$ and $NdNi_4Mg$ [J]. Journal of Alloys and Compounds, 2003, 348(1−2): 129−137.

[6] WANG Z M, ZHOU H Y, GU Z F, CHENG G, YU A B. Preparation of $LaMgNi_4$ alloy and its electrode properties [J]. Journal of Alloys and Compounds, 2004, 377(1−2): L7−L9.

[7] LIU Y F, CAO Y H, HUANG L, GAO M X, PAN H G. Rare earth–Mg−Ni-based hydrogen storage alloys as negative electrode materials for Ni/MH batteries [J]. Journal of Alloys and Compounds, 2011, 509(3): 675−686.

[8] ZHANG Y H, HAN Z G, YANG Z M, YANG T, QI Y, ZHAO D L. Electrochemical properties of nanocrystalline and amorphous Mg−Y−Ni alloys applied to Ni−MH battery [J]. Transactions of Nonferrous Metals Society of China, 2015, 25(11): 3736−3746.

[9] YANG T, YUAN Z M, BU W G, JIA Z C, QI Y, ZHANG Y H. Effect of elemental substitution on the structure and hydrogen storage properties of $LaMgNi_4$ alloy [J]. Materials & Design, 2016, 93: 46−52.

[10] CASINI J C S, GUO Z P, LIU H K, FERREIRA E A, FARIA R N, TAKIISHI H. Effect of Sn substitution for Co on microstructure and electrochemical performance of AB_5 type $La_{0.7}Mg_{0.3}Al_{0.3}Mn_{0.4}Co_{0.5-x}Sn_xNi_{3.8}$ (x=0−0.5) alloys [J]. Transactions of Nonferrous Metals Society of China, 2015, 25(2): 520−526.

[11] YANG T, ZHAI T T, YUAN Z M, BU W G, XU S, ZHANG Y H. Hydrogen storage properties of $LaMgNi_{3.6}M_{0.4}$ (M=Ni, Co, Mn, Cu, Al) alloys [J]. Journal of Alloys and Compounds, 2014, 617: 29−33.

[12] ZHANG Y H, LI P X, YANG T, ZHAI T T, YUAN Z M, GUO S H. Effects of substituting La with M (M=Sm, Nd, Pr) on electrochemical hydrogen storage characteristics of A_2B_7-type electrode alloys [J]. Transactions of Nonferrous Metals Society of China, 2014, 24(12): 4012−4022.

[13] KNOTEK V, VOJTĚCH D. Electrochemical hydriding performance of Mg–TM−Mm (TM=transition metals, Mm=mischmetal) alloys for hydrogen storage [J]. Transactions of Nonferrous Metals Society of China, 2013, 23(7): 2047−2059.

[14] ZHANG Y H, XU S, ZHAI T T, YANG T, YUAN Z M, ZHAO D L. Hydrogen storage kinetics of nanocrystalline and amorphous Cu−Nd-added Mg_2Ni-type alloys [J]. Transactions of Nonferrous Metals Society of China, 2014, 24(11): 3524−3533.

[15] ZHANG Y H, CAI Y, ZHAO C, ZHAI T T, ZHANG G F, ZHAO D L. Electrochemical performances of the as-melt $La_{0.75-x}M_xMg_{0.25}Ni_{3.2}Co_{0.2}Al_{0.1}$ (M=Pr, Zr; x=0, 0.2) alloys applied to Ni/metal hydride (MH) battery [J]. International Journal of Hydrogen Energy, 2012, 37(19): 14590−14597.

[16] ZHANG Y H, YUAN Z M, YANG T, HOU Z H, ZHAO D L. Properties of mechanically milled nanocrystalline and amorphous Mg−Y−Ni electrode alloys for Ni–MH batteries [J]. Acta Metallurgica Sinica (English Letters), 2015, 28(7): 826−836.

[17] ZÜTTEL A. Materials for hydrogen storage [J]. Materials Today, 2003, 6(9): 24−33.

[18] WU M S, WU H R, WANG Y Y, WAN C C. Surface treatment for hydrogen storage alloy of nickel/metal hydride battery [J]. Journal of Alloys and Compounds, 2000, 302(1−2): 248−257.

[19] ORIMO S, FUJII H. Materials science of Mg−Ni-based new hydrides [J]. Applied Physics A, 2001, 72(2): 167−186.

[20] LAI W H, YU C Z. Research survey of improving discharge voltage platform for Ni−MH battery [J]. Battery Bimonthly, 1996, 26(4): 189−191.

[21] WU Y, HAN W, ZHOU S X, LOTOTSKY M V, SOLBERG J K, YARTYS V A. Assessment of the diffusional mobilities in bcc Ti−V alloys [J]. Journal of Alloys and Compounds, 2009, 470(1−2): 176−182.

[22] ZHAI T T, YANG T, YUAN Z M, ZHANG Y H. An investigation on electrochemical and gaseous hydrogen storage performances of as-cast $La_{1-x}Pr_xMgNi_{3.6}Co_{0.4}$ (x=0−0.4) alloys [J]. International Journal of Hydrogen Energy, 2014, 39(26): 14282−14287.

[23] MA Z W, ZHOU W H, WU C L, ZHU D, HUANG L W, WANG Q N, TANG Z Y, CHEN Y G. Effects of size of nickel powder additive on the low-temperature electrochemical performances and kinetics parameters of AB_5-type hydrogen storage alloy for negative electrode in Ni/MH battery [J]. Journal of Alloys and Compounds, 2016, 660: 289−296.

[24] ZHAO X Y, DING Y, MA L Q, WANG L Y, YANG M, SHEN X D. Electrochemical properties of $MmNi_{3.8}Co_{0.75}Mn_{0.4}Al_{0.2}$ hydrogen storage alloy modified with nanocrystalline nickel [J]. International Journal of Hydrogen Energy, 2008, 33(22): 6727−6733.

[25] ZHENG G, POPOV B N, WHITE R E. Electrochemical determination of the diffusion coefficient of hydrogen through a $LaNi_{4.25}Al_{0.75}$ electrode in alkaline aqueous solution [J]. Journal of the Electrochemical Society, 1995, 142(8): 2695−2698.

[26] KURIYAMA N, SAKAI T, MIYAMURA H, UEHARA I, ISHIKAWA H, IWASAKI T. Electrochemical impedance and deterioration behavior of metal hydride electrodes [J]. Journal of Alloys and Compounds, 1993, 202(1−2): 183−197.

[27] KLEPERIS J, WÓJCIK G, CZERWINSKI A, SKOWRONSKI J, KOPCZYK M, BELTOWSKA-BRZEZINSKA M. Electrochemical behavior of metal hydrides [J]. Journal of Solid State Electrochemistry, 2001, 5(4): 229−249.

快淬对 RE−Mg−Ni−Mn 系 AB_2 型贮氢合金结构及电化学性能的影响

张羊换[1,2]，张 巍[1]，宋希平[3]，张沛龙[3]，朱永国[3]，祁 焱[2]

1. 内蒙古科技大学 内蒙古自治区白云鄂博矿多金属资源综合利用重点实验室，包头 014010；
2. 钢铁研究总院 功能材料研究所，北京 100081；
3. 北京浩运金能科技有限公司，北京 100083

摘 要：为了提高合金的电化学性能，采用 Ce 部分替代 La，并结合快淬方法制备了 $La_{1-x}Ce_xMgNi_{3.5}Mn_{0.5}$ (x=0, 0.1, 0.2, 0.3, 0.4)贮氢合金。XRD 和 SEM 测试结果表明，合金由 $LaMgNi_4$ 主相以及 $LaNi_5$ 第二相组成。随着快淬速度的增加，合金的晶格参数及晶胞体积逐渐增大，晶粒明显得到细化。电化学测试结果表明，铸态及快淬态合金具有优异的活化性能，其放电容量均在第一次循环时即可达到最大值。随着快淬速度的增加，合金的放电容量先增大后减小，但其循环稳定性逐渐提高。此外，合金电极的电化学动力学性能均随快淬速度的增加先提高后降低。

关键词：镍氢电池；贮氢；快淬；放电容量；动力学

(Edited by Wei-ping CHEN)